communications biology

A Nature Portfolio journal

Article

https://doi.org/10.1038/s42003-025-08704-6

Single-dose infusion of engineered viral receptor binding domain confers rapid and durable protection against viral infection

Haiqiao Sun[1,8], Bei Tong[2,8], Deshan Ren[1,8], Ao Hu[3,8], He Li[1], Yixin Zhang[3], Shuang Liu[1], Xiang Duan[1], Zijian Zhang[1], Wei Liu[1], Haokun Yang[4], Jian Chen[2], Tunyu Jian[2], Huanying Zheng[5], Bixia Ke[5], Hanri Zeng[5], Changwen Ke[5], Xiaofang Peng[5], Yongzhen Liu[1], Kai Deng[3] ✉, Xianchi Dong[4] ✉ & Yan Li[1,6,7] ✉

Developing both rapid- and long-acting antiviral drugs for single-dose administration can improve medication adherence and protect people at risk of infection. To provide proof of this concept, here, we designed multimerized form of viral receptor-binding domains (RBDs) to immediately occupy viral receptors to block infection and subsequently induce virus-specific protective immunity. We engineered SARS-CoV-2 RBD, enhancing its affinity to ACE2 and immunogenicity through multimerization and Fc modification. A single administration of 4RBD-Fc not only effectively blocked ACE2-dependent SARS-CoV-2 infections but also elicited robust virus-specific mucosal and systemic immunity in the absence of adjuvants, providing superior early and long-lasting protection compared to adjuvanted vaccines in mice. These findings demonstrate the feasibility and efficacy of engineered viral RBD as immediate-acting and long-lasting single-dose antiviral drugs through rapid receptor blocking and ensuing adaptive immunity induction.

Certain viral infections are initiated by events that individuals can be aware of, such as insect bites (dengue fever), animal bites (rabies), unprotected sexual activities and sharing injection needles (HIV, HCV), and community outbreaks (respiratory viruses). In these scenarios, proactive use of antiviral drugs for pre-exposure prophylaxis (PrEP) or post-exposure prophylaxis (PEP) can prevent infection[1–5]. However, taking HIV PEP as an example, due to the short efficacy of antiretroviral drugs and the need for repeated dosing, adherence to the 28-day PEP regimen has historically been low, leading to reduced prevention[6–8]. Fewer medical interventions, such as reducing multiple daily doses to once a day[9,10], and extending the duration of antiviral drug efficacy, such as with the long-term antiviral drug cabotegravir[5], help improve medication compliance and preventive outcomes. Therefore, there is an urgent need to develop both immediate- and long-acting antiviral drugs for single-dose administration. Indeed, during the pandemic, such agent is also needed for providing immediate and long-lasting protection to vulnerable population.

To initiate the infection cycle, viral particles must use viral surface proteins to interact with viral receptors on the cell, in order to achieve viral attachment or membrane-fusion[11]. Therefore, using the fusion protein or their components may pre-emptively occupy viral receptors and exert an antiviral effect. For example, antiviral peptides derived from the gp120 (185-192) on HIV (peptide T) can bind to CCR5 to block HIV infection of $CD4^+$ T cells[12,13]. We propose that using the entire viral receptor binding domain (RBD) instead of virus-derived peptides could stimulate greater antibody responses, as peptides generally have weaker immunogenicity for humoral immunity[14]. In this context, the antiviral effect of viral RBDs can be maintained and extended by the activated adaptive immune system. This concept, to our knowledge, has not been explored in vivo before, and thus

[1]MOE Key Laboratory of Model Animal for Disease Study, Model Animal Research Center, Department of Oncology, Nanjing Drum Tower Hospital, Affiliated Hospital of Medical School, Nanjing University, Nanjing, 210061, China. [2]Jiangsu Key Laboratory for the Research and Utilization of Plant Resources, Institute of Botany, Jiangsu Province and Chinese Academy of Sciences, Nanjing, 210014, China. [3]MOE Key Laboratory of Tropical Disease Control, Department of Immunology and Microbiology, Advanced Medical Technology Center, The First Affiliated Hospital, Zhongshan School of Medicine, Sun Yat-sen University, Guangzhou, 510275, China. [4]State Key Laboratory of Pharmaceutical Biotechnology, School of Life Sciences, Nanjing University, Engineering Research Center of Protein and Peptide Medicine, Ministry of Education, Nanjing, 210023, China. [5]Guangdong Provincial Center for Disease Control and Prevention, Guangzhou, 510060, China. [6]ChemBioMed Interdisciplinary Research Center at Nanjing University, Nanjing, 210061, China. [7]Wuxi Xishan NJU Institute of Applied Biotechnology, Wuxi, 214101, China. [8]These authors contributed equally: Haiqiao Sun, Bei Tong, Deshan Ren, Ao Hu. ✉e-mail: dengkai6@mail.sysu.edu.cn; xianchidong@nju.edu.cn; yanli@nju.edu.cn

our work represents an initial proof-of-concept effort to evaluate its feasibility and potential advantages over conventional antiviral strategies.

SARS-CoV-2 virus was chosen as our prototype for concept testing since it has a clear RBD (amino acids 319-541 on the Spike protein) and interacts with the viral receptor ACE2 with nM affinity[15,16]. Meanwhile, the RBD of SARS-CoV-2 contains multiple immunodominant epitopes that can elicit a potent antibody response and induce the production of neutralizing antibodies[16–18]. On the other hand, since SARS-CoV-2 infects through mucosal routes[19], testing whether this drug can be administered via the respiratory route to activate mucosal immunity is an intriguing idea since inhalation has better adherence compared to injection, and mucosal vaccines have shown better clinical outcome in many studies due to their ability to elicit effective mucosal immunity at the site of infection like mucosal antibodies and tissue-resident immune cells[20,21].

To achieve the goal of preempting viral receptors and activating the immune system, the SARS-CoV-2 RBD needs to be engineered with a higher affinity for ACE2 than its natural counterpart, while maintaining its sequence to preserve immunogenicity. Meeting this requirement is the multimerization to enhance receptor-binding affinity[22]. Additionally, to effectively activate the immune system, the drug must cross the mucosal barrier to reach lymphatic tissue. Recombinant protein fused with a Fc region from human IgG has been demonstrated to bind neonatal Fc receptors (FcRn) on epithelial cells, facilitating their transportation into tissue[23–25]. Therefore, multimerization and Fc fusion may enhance the receptor-blocking effect and immune activation capacity of RBD-based antiviral drugs.

To develop a single-dose long-acting antiviral drug against SARS-CoV-2, we optimized RBD's binding capacity for ACE2 and immunogenicity to competitively block virus entry while simultaneously activating an anti-RBD immune response in the respiratory mucosa, where SARS-CoV-2 initially infects host cells. Through structure-based protein design, we generated an RBD multimer, named 4RBD-Fc, with higher binding affinity towards ACE2 and stability than other RBD constructs. Pre-incubating 4RBD-Fc with ACE2-expressing cell lines can block the infection of multiple SARS-COV-2 variants. Intranasal (i.n.) administration of 4RBD-Fc to K18-hACE2 mice persisted in pulmonary tissues for at least 7 days post-administration. Notably, prophylactic treatment with 4RBD-Fc could protect K18-hACE2 mice from the lethal SARS-CoV-2 Delta variant infection. Additionally, after i.n. administration, 4RBD-Fc selectively drains to respiratory-associated lymphoid tissues, activating a de novo immune response against RBD, providing a more robust systemic and mucosal immune response than traditional mucosal vaccines with adjuvants. SARS-CoV-2 challenge in K18-hACE2 mice experimentally verified that a single dose treatment of 4RBD-Fc in the absence of adjuvant could offer a stronger anti-viral effect than multiple doses of conventional vaccines. Given the lack of prior in vivo investigations into the use of viral RBDs as receptor-blocking prophylactic agents, this study is exploratory in nature and aims to provide proof-of-concept evidence for the design, delivery, and efficacy of such agents. This dual-function strategy supports the further development of viral RBDs as both pre-exposure and post-exposure prophylactic interventions against viral infections.

Results

Structure-based RBD multimer design to enhance stability and human ACE2 binding affinity

Extensive characterization of spike protein residues 319-541, previously considered the RBD required for human ACE2 (hACE2) binding[26,27], showed that this recombinant RBD protein fragment tends to dimerize, potentially forming higher-order multimers, due to the presence of an unpaired cysteine residue (C538) close to the C-terminus[16,28]. To prevent this dimerization activity in our constructs, we used a previously reported cryo-electron microscopy structure (PDB ID: 6VXX) to design a longer truncated RBD spanning residues 319-591 that allows formation of disulfide bonds between C538 and C590 (Fig. 1A)[16]. Subsequent molecular dynamics (MD) simulations showed that RBD (319-591) was more stable than RBD (319-541), and had a lower RMSD than that of RBD (319-541) (RMSD = 2.5 Å versus ~5 Å, RBD (319-591) versus RBD (319-541); Fig. 1B), we therefore used RBD (319-591) in the following experiments.

In order to counteract the binding of the trimeric SARS-CoV-2 spike protein to the hACE2 receptor, the recombinant RBD needs to exhibit high affinity towards hACE2. To achieve this, we engineered several RBD (319–591) constructs, including a monomer, a set of oligomers (2–3 RBD units in length), and a set of oligomers (2–4 RBD units) fused to a human IgG1 Fc domain (Fig. 1A), as attempts to incorporate additional RBD copies led to significantly reduced protein yields. We then verified their size and purity through SDS-PAGE and size-exclusion chromatography (Fig. 1C and Supplementary Fig. 1A).

Characterization of the tertiary structure of 4RBD-Fc by negative-stain electron microscopy (EM) revealed that it tends to form a beads-on-a-string-like architecture, with multiple RBD subunits loosely arranged around a central base, suggesting the dimerization of two 4RBD-Fc molecules (Fig. 1D). Each RBD subunit appeared intact and was connected via flexible glycine–serine linkers, while the central base was composed of two dimerized human IgG1 Fc domains. Due to the flexible linkers, the exact orientation of the receptor-binding motifs (residues 437–508) could not be precisely resolved; however, the arrangement appears compatible with accessibility for ACE2 binding.

To probe interactions between the RBD oligomers and hACE2, we next conducted cell-surface-binding assays using flow cytometry. Series-diluted RBD constructs were incubated with hACE2-expressing cell line (293T-hACE2) in the presence of 100 nM AlexaFluor 488-labeled RBD protein. This analysis revealed that the K_d value of RBD monomer was 36.6 ± 10.2 nM, whereas the K_d values for the oligomers were 1.7 ± 0.5 nM (2RBD), 1.4 ± 0.4 nM (3RBD), 4.8 ± 1.4 nM (RBD-Fc), 2.7 ± 0.8 nM (2RBD-Fc), 1.9 ± 0.6 nM (3RBD-Fc), and 0.8 ± 0.2 nM (4RBD-Fc) (Fig. 1E). 3RBD in the RBD oligomers and 4RBD-Fc in the Fc-fused RBD oligomers exhibit the two strongest binding capability for hACE2, being 26-fold and 46-fold higher than the RBD monomer, respectively. Therefore, they were chosen for further experiments. These results suggested that the oligomeric and Fc-fused RBD proteins retained the functionality of native RBD and could potentially interact with ACE2 more robustly.

Evaluation of 4RBD-Fc as an effective broad-spectrum blocker for SARS-CoV-2 variants in vitro

The inhibitory effects of RBD oligomers on viral entry was assessed using SARS-CoV-2 pseudovirus blocking assays. 293T-hACE2 cells, pre-incubated with RBD oligomers and then infected with a luciferase-reporter pseudovirus displaying the wild-type (WT) SARS-CoV-2 spike protein[29], exhibited reduced luminescence compared to non-pre-incubated cells, suggesting inhibition of spike protein-mediated entry. Dose-dependent luminescence reduction post-infection was observed with RBD monomer, 3RBD, and 4RBD-Fc (Fig. 1F), while 4RBD-Fc showed the highest inhibition (IC_{50} = 0.27 ± 0.08 nM), outperforming both RBD monomer (IC_{50} = 4.7 ± 1.5 nM) and 3RBD (IC_{50} = 0.27 ± 0.08 nM). Consequently, 4RBD-Fc was selected for further study.

Acknowledging the limitation of pseudovirus studies, we further extended our investigation to clinically isolated SASR-CoV-2 viruses using Vero E6 cells in a biosafety level 3 (BSL-3) laboratory. Similar to the results of pseudovirus blocking assays, 4RBD-Fc pre-incubation effectively reduced viral load (measured by qRT-PCR) in Vero E6 cells infected with WT SARS-CoV-2 and two variants, including Delta (B.1.617.2) and BA.2 (B.1.1.529.2), with IC_{50} of 17.3 ± 4.3 nM, 5.2 ± 4.2 nM, and 11.6 ± 5 nM, respectively (Fig. 1G). These outcomes suggest that the interaction of 4RBD-Fc with ACE2 effectively blocks the entry of various SARS-CoV-2 variants in vitro. Overall, these results demonstrate the exceptional blocking activity of 4RBD-Fc for SARS-CoV-2 among the other RBD constructs, and its potential as a broad-spectrum antiviral agent for SARS-CoV-2 variants.

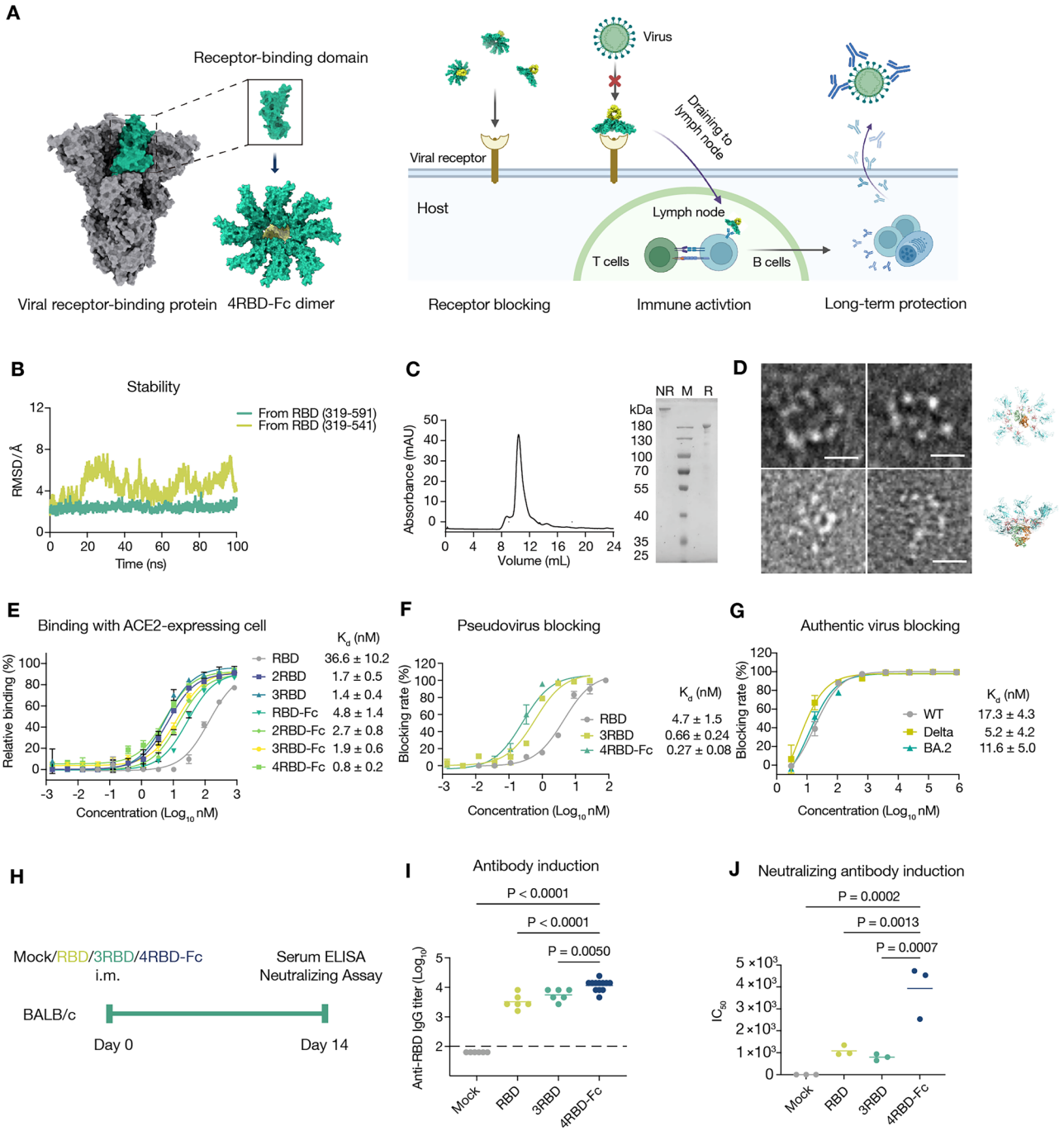

Fig. 1 | Characterizing of engineered RBD constructs. A Schematic of the 4RBD-Fc design. Four serially connected RBD (amino acid residues 319-591 of SARS-CoV-2 spike protein, green) were fused to a human IgG1 Fc domain at the C-terminal (yellow), with two 4RBD-Fc monomers forming a dimer. **B** The stability of RBD (319-591) and RBD (319-541) was compared by computing the backbone RMSD of the entire trajectories, carried out by VMD software. RMSD, root mean square deviation. **C** SDS-PAGE (left) of the eluted 4RBD-Fc samples, showing 4RBD-Fc assembly and purity. Size exclusion chromatography analysis of 4RBD-Fc (right). The ultraviolet absorption at 280 nm were shown. mAU, milli-absorbance units. M, marker; NR, non-reducing; R, reducing. **D** Representative raw images of 4RBD-Fc from negative-stain EM were shown. (Scale bar: 10 nm). Schematic of 4RBD-Fc dimer are shown to the right. **E** Competitive cell-surface binding of different RBD constructs. Relative binding (%) is calculated by measuring the reduction in mean fluorescence intensity (MFI) from RBD-FITC through flow cytometry. K_d values were calculated using the Cheng-Prusoff equation. K_d values were shown. **F** SARS-CoV-2 pseudovirus blocking assay. 293T-hACE2 cells were pre-incubated with serially diluted concentrations of RBD, 3RBD, or 4RBD-Fc and then infected with a luciferase-reporter SARS-CoV-2 pseudovirus. Blocking rate is calculated as the percent reduction in luminescence relative to control cells, which were not pre-incubated. **G** SARS-CoV-2 authentic virus blocking assay. VeroE6 cells were pre-incubated with 4RBD-Fc at indicated concentrations then infected with clinical isolated SARS-CoV-2 variants, the blocking rate is calculated as the percent reduction in viral load relative to control cells, measured by quantitative PCR with reverse transcription (qRT-PCR). Non-linear three-parameters inhibitor-response curve was used to determine the IC_{50} values. **H** BALB/c mice were i.m. immunized with RBD ($n = 7$), 3RBD ($n = 7$) or 4RBD-Fc ($n = 12$) as indicated and all adjuvanted with Alum and CpG, while mock group i.m. immunized with Alum and CpG only ($n = 6$), mice were sacrificed at 14 days-post immunization. **I** Serum was collected at day 14 for analysis, and anti-RBD IgG antibody titers were measured by ELISA. Endpoint titers were presented. **J** Neutralizing assay of day 14 serum in (**H**) use SARS-CoV-2 WT pseudovirus. IC_{50} was shown. Data are presented as mean ± s.d. The dashed line indicates the limit of detection (LOD). Undetectable values were set to LOD − 0.2 log units to distinguish them.

Immunogenicity assessment of RBD oligomers

Next, we assessed whether these RBD oligomers retained immunogenicity by testing a single dose of intramuscular (i.m.) immunization with 10 μg of RBD, 3RBD, or 4RBD-Fc antigens in BALB/c mice, using CpG and aluminum hydroxide gel (Alum) as adjuvants. Serum samples were then collected for antibody titers and pseudovirus neutralization analysis (Fig. 1H). Enzyme-linked immunosorbent assay (ELISA) analysis of anti-RBD IgG antibodies in serum revealed that the 4RBD-Fc group exhibited the highest antibody titers (1×10^4), surpassing those of the RBD (3.2×10^3) and 3RBD groups (5×10^3) (Fig. 1I). Additionally, pseudovirus neutralization assays demonstrated that serum from the 4RBD-Fc group had a significantly higher neutralization capacity against WT SARS-CoV-2 pseudovirus ($IC_{50} = 3934$) compared to the RBD ($IC_{50} = 1086$) and 3RBD groups ($IC_{50} = 796.8$) (Fig. 1J). These data suggest that the RBD oligomers retained their immunogenicity, with 4RBD-Fc generating stronger binding and neutralizing antibody levels compared to RBD and 3RBD.

Restricted 4RBD-Fc distribution in the respiratory system avoids inducing inflammation or allergic reactions

To assess the suitability of 4RBD-Fc as an antiviral agent, we investigated its in vivo distribution kinetics via i.n. administration of 1 mg AlexaFluor 750-labeled 4RBD-Fc (4RBD-Fc-AF750) to K18-hACE2 mice (Fig. 2A). Given that murine ACE2 receptor does not bind to the RBD of SARS-CoV-2[30], we employed K18-hACE2 mice, which express hACE2 driven by the cytokeratin-18 (K18) promoter in epithelial cells[31]. Bioimaging of whole mice in vivo and in ex vivo dissected organs showed that 4RBD-Fc rapidly localized to lungs within 4 hours (Fig. 2B–E) and remained detectable in both the upper and lower respiratory tract (Fig. 2C, D) for at least 168 hours (Fig. 2B, E), indicating high stability of 4RBD-Fc in the respiratory tract microenvironment. During the initial 96 hours post-administration, the AF750 signal in the bioimaging data was confined to the respiratory tract, suggesting restricted localization of the 4RBD-Fc (Supplementary Fig. 2A–C). However, at 96 hours post-administration, 4RBD-Fc signal could be observed in ex vivo liver and kidney tissues, suggesting possible degradation or transport of 4RBD-Fc (Supplementary Fig. 2B, C). Importantly, by 336 hours (14 days) post-administration, AF750 signals had become undetectable in the respiratory tract in the majority of mice, with only one mouse showing a faint signal in the nasal cavity and lungs—demonstrating effective clearance of the protein from the respiratory system over time (Fig. 2E). Overall, these findings indicate that 4RBD-Fc exhibits strong and specific localization to the respiratory tract at early stage, prolonged local stability, and minimal systemic exposure, making it a promising candidate for intranasal antiviral therapy.

To further assess the safety of intranasally administered 4RBD-Fc, we conducted both pulmonary and systemic evaluations in K18-hACE2 mice. Mice were intranasally administered with either 1 mg of 4RBD-Fc or an equal volume of PBS (vehicle control) (Supplementary Fig. 3A). Throughout the 7-day observation period, mice were monitored daily for body weight, behavior (including activity and grooming), and general appearance (fur condition and posture), and no adverse clinical signs were observed in the 4RBD-Fc-treated group compared to the vehicle group. At 7 days post-administration, flow cytometry analysis of lung single-cell suspensions showed no significant difference in immune cell infiltration, including total leukocytes and four types of granulocytes (neutrophils, eosinophils, basophils, and mast cells), between the two groups (Supplementary Fig. 3B).

Given that allergic reactions are characterized not only by eosinophil infiltration but also by T helper type 2 (Th2) immune responses, we further employed an in vitro RBD peptide library stimulation method to assess the presence of RBD-specific Th2 cells. Lung cells were stimulated with the RBD peptide library for 6 hours, followed by intracellular cytokine staining and flow cytometric detection of $CD3^+CD4^+IL\text{-}4^+$ cells (Supplementary Fig. 3C). No significant difference in pulmonary Th2 cell frequency was observed between groups (Supplementary Fig. 3D), suggesting that intranasal 4RBD-Fc did not trigger a Th2-skewed immune response. These findings demonstrate that intranasal administration of 4RBD-Fc did not induce pulmonary inflammation, allergic reactions, or systemic toxicity in vivo.

Prophylactic and therapeutic effects of i.n. administered 4RBD-Fc in SARS-CoV-2-infected mice

To assess the antiviral activity of 4RBD-Fc as a preventive or therapeutic treatment for SARS-CoV-2, we administered 4RBD-Fc (1 mg i.n.) or the PBS vehicle control to K18-hACE2 mice at either 2 hours before (PrEP group) or 24 or 48 hours after (PEP group) infection with the SARS-CoV-2 Delta strain with 4×10^3 plaque-forming units (PFU) per mouse (Fig. 2F), as a well-established infection system[32]. At 5 days post-infection (dpi), significant weight loss (21.5%) was observed in the vehicle group, with all animals being euthanized by 5 dpi (a ≥ 15% loss of body weight compared to baseline was considered as the humane endpoint) (Fig. 2G). In contrast, all mice in the PrEP group and 66.7% (4/6) of the mice in the PEP group survived at 5 days post-infection (dpi). Both PrEP and PEP groups showed markedly lower viral loads in the upper respiratory tract (lower than LOD in PrEP, 2.8×10^3 copies/ml in PEP versus 8.3×10^4 copies/ml in vehicle controls) and lower respiratory tract (lower than LOD in PrEP, 3.1×10^4 copies/ml in PEP versus 8×10^7 copies/ml in vehicle controls), as confirmed by viral titer assays of throat swabs and lung tissues. Complete viral clearance (viral load < limit of detection: 1×10^3 copies/ml) was achieved in 66.7% (2/3) of the PrEP group (Fig. 2H, I). These results thus supported that 4RBD-Fc administration could effectively reduce viral load of the SARS-CoV-2 Delta variant in vivo.

Given these findings, we next evaluated whether 4RBD-Fc affected transmission of SARS-CoV-2. Index mice, infected with the Delta strain at 4×10^4 PFU, ten-fold higher than lethal concentrations, were co-housed with contact mice treated with 4RBD-Fc or PBS vehicle. By 5 dpi, all index mice succumbed, whereas none died in the contact groups (Fig. 2J). Viral titer assays indicated that vehicle-treated contact mice had obvious accumulation of viral loads (8×10^3 copies/ml in throat swabs and 2.6×10^4 copies/ml in lungs at 5 dpi) following contact with the index group (Fig. 2K), whereas no virus (below limit of detection) was detected in the 4RBD-Fc contact group by 5 dpi. These data were consistent with viral titer assays from throat swabs and lung tissue samples by 5 dpi (Fig. 2K, L). However, we observed detectable viral titers in the throat swabs of one mouse in the 4RBD-Fc contact group at both 1 dpi and 3 dpi.

Histopathological examination of the vehicle controls and index groups revealed diffuse hemorrhage, severe alveolar thickening, and bronchiole structure loss, indicative of fatal pneumonia progression, whereas only mild alveolar thickening was noted in the vehicle-treated contact groups (Supplementary Fig. 4A). Notably, no lung lesions were observed in the PrEP and 4RBD-Fc-treated contact groups. Altogether, these results advocate for the potential of i.n. delivered 4RBD-Fc as both prophylactic and therapeutic agent against SARS-CoV-2 infection and transmission.

Activation of anti-RBD de novo immune responses in respiratory-associated lymphoid tissues via i.n. administration of unadjuvanted 4RBD-Fc

Next, we examined the ability of 4RBD-Fc to drain to lymph nodes after i.n. administration. We assessed the distribution of 4RBD-Fc-AF750 in secondary lymphoid organs of K18-hACE2 mice (Fig. 3A). After 1 mg 4RBD-Fc-AF750 i.n. administration, 4RBD-Fc rapidly drained to respiratory-associated lymphoid tissues such as nasal-associated lymphoid tissues (NALT), mandibular lymph nodes (maLN), and mediastinal lymph nodes (mdLN) (Fig. 3B, C), but not to other secondary lymphoid tissues at early time points (Supplementary Fig. 4A–C). The 4RBD-Fc-AF750 signal in lymphoid tissues progressively rose, showing a 15.7-fold (NALT), 22.7-fold (maLN), and 12.6-fold (mdLN) increase by 96 hours, and a 17.2-fold (NALT), 60.1-fold (maLN), and 41.7-fold (mdLN) increase by 168 hours compared to 48 hours, indicating active accumulation of 4RBD-Fc in respiratory-associated lymphoid tissues by 96 hours (Fig. 3B). In addition, at 96 and

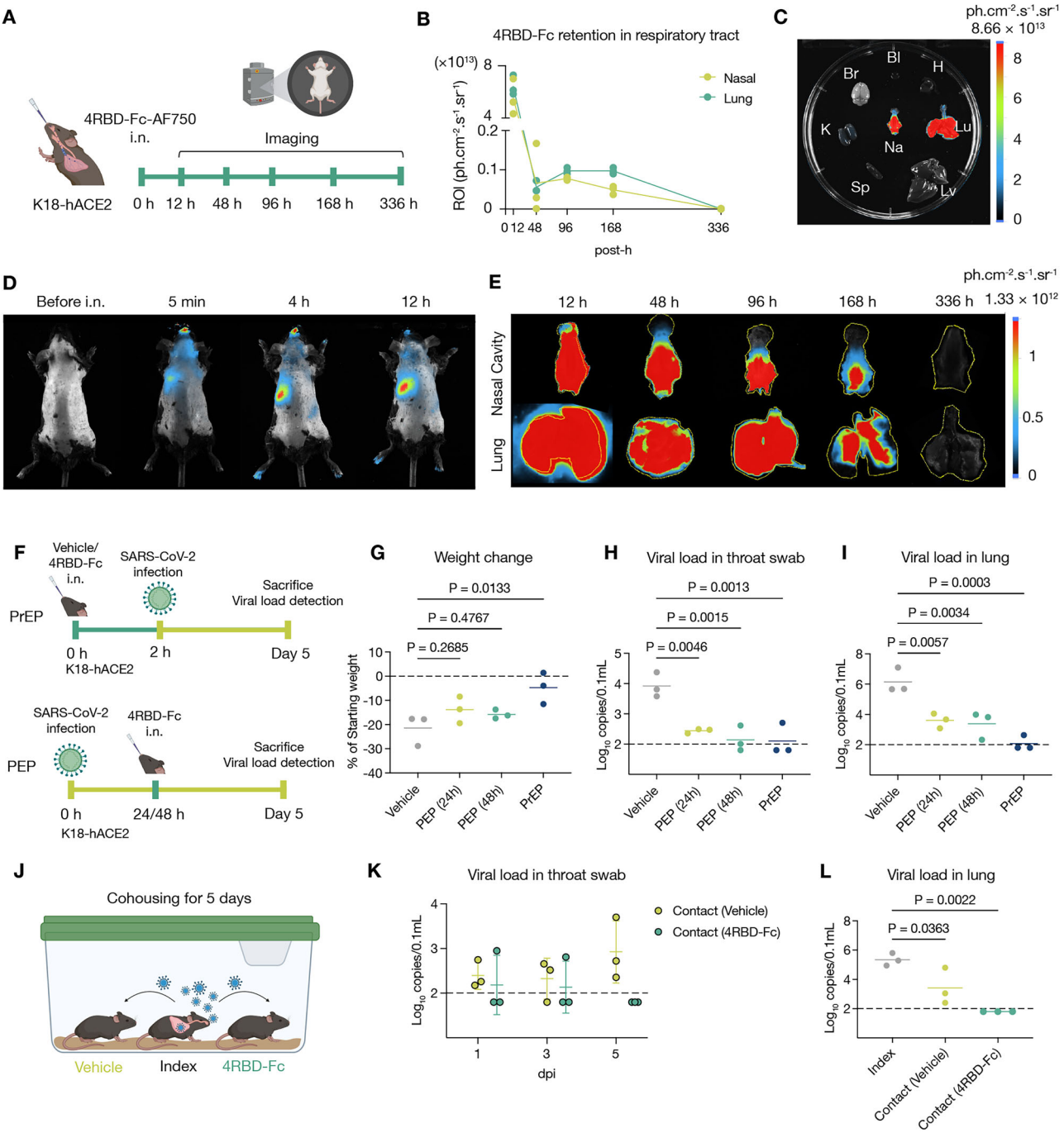

Fig. 2 | 4RBD-Fc treatment prevents SARS-CoV-2 infection in either prophylactic or therapeutic use. A Schematic illustrating the experimental design to assess the bio-distribution of 4RBD-Fc. **B** Quantitative analysis of AF750 fluorescence signals in nasal cavity and lung at different post-hours (post-h). **C, D** Representative ex vivo images of dissected organs (**C**), representative whole-body images (**D**). Abbreviations: Bl, blood (20 μl); Br, brain; H, heart; K, kidney; Lu, lung; Lv, liver; Na, nasal cavity; S, spleen. **E** Representative ex vivo dynamic imaging of AF750 fluorescence changes in the nasal cavity and lung. **F** A SARS-CoV-2 infection protocol using K18-hACE2 mice. In PrEP experiment mice were i.n. administrated with 1 mg 4RBD-Fc or vehicle (equal volume of PBS), then infected with 4×10^3 PFU SARS-CoV-2 Delta strain. In PEP experiment, mice were infected with 4×10^3 PFU SARS-CoV-2 Delta strain, then received 1 mg 4RBD-Fc i.n. at 24- or 48-hours post-infection. **G** Relative weight was measured as a percent of the starting weight on day 5 after infection with SARS-CoV-2 Delta strain ($n = 3$). The dashed line indicates the starting weight. Viral loads in throat swaps (**H**) and in the lungs (**I**) were detected by qRT-PCR. **J** A SARS-CoV-2 transmission protocol using K18-hACE2 mice ($n = 3$). Mice were infected with 4×10^4 PFU of the Delta strain (index group) and then co-housed for 5 days with two other groups (contact group), which were i.n. administered 1 mg 4RBD-Fc or a vehicle (equal volume of PBS) 2 hours before co-housing. Viral load in throat (**K**) and lungs (**L**) was detected by qRT-PCR. The dashed line indicates the limit of detection (LOD). Undetectable values were set to LOD − 0.2 log units to distinguish them. Statistical significance was calculated by one-way ANOVA with Dunnett correction. Data are presented as mean ± s.d.

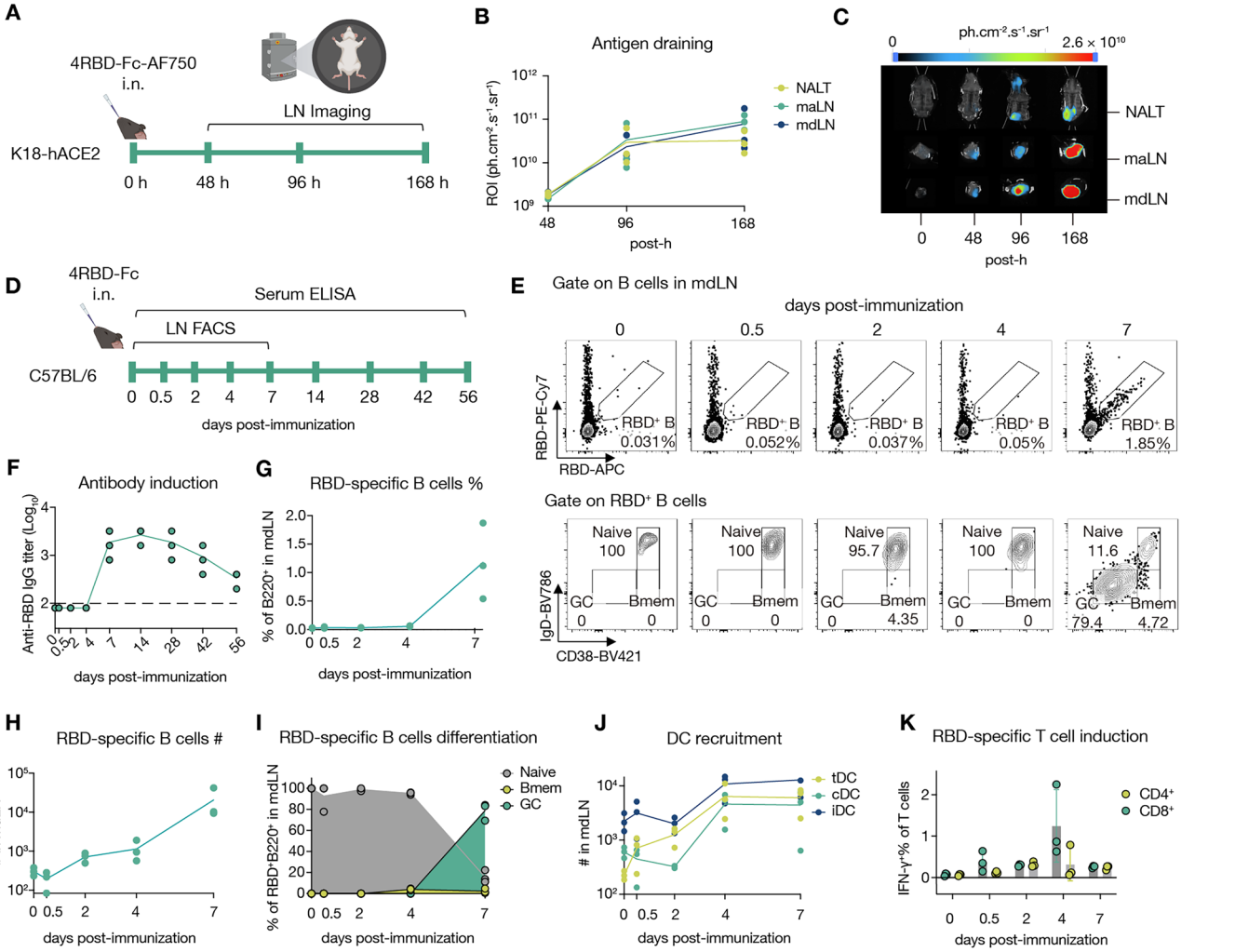

Fig. 3 | I.n. administration of 4RBD-Fc elicits anti-RBD de novo immune responses in respiratory-associated lymphoid tissues. A Schematic of the experimental design for evaluating the drainage of 4RBD-Fc to secondary lymphoid tissues after i.n. administration ($n = 3$). **B** Quantitative analysis of 4RBD-Fc presence in respiratory-associated lymphoid tissues. NALT, Nasal-Associated Lymphoid Tissue; maLN, Mandibular Lymph Nodes; mdLN, Mediastinal Lymph Nodes. **C** Representative images showing the distribution of 4RBD-Fc-AF750 in respiratory-associated lymphoid tissues. **D** Schematic representation of the immune response dynamics following 1 mg i.n. administration of 4RBD-Fc in C57BL/6 mice ($n = 3$). **E** Representative flow cytometry plots of the kinetics of RBD-specific B cell responses in mediastinal lymph nodes (mdLN), RBD^+ B cells are defined as ($B220^+RBD\text{-}PE\text{-}Cy7^+RBD\text{-}APC^+$). RBD^+ B cell are differentiated from naïve B cell (Naïve, $CD38^+IgD^+$) to memory B cell (Bmem, $CD38^+IgD^-$) and germinal center B cell (GC B, $CD38^-IgD^-$). **F** Anti-RBD IgG antibodies titers in serum at dynamic timepoint, measured via ELISA ($n = 3$). The dashed line indicates the limit of detection (LOD). Undetectable values were set to LOD −0.2 log units to distinguish them. Quantitative analyses of RBD-specific B cell responses in mdLN, including RBD^+ B cells percentage (**G**) and numbers (**H**). **I** Quantitative analyses of RBD^+ B cell differentiation in mdLN at dynamic timepoint. **J** The dynamics of DC subsets in mdLN following i.n. administration of 4RBD-Fc. cDC ($MHC\text{-}II^+CD11c^{hi}$), iDC ($MHC\text{-}II^+CD11c^{lo}$), tDC ($MHC\text{-}II^{hi}CD11c^+$). **K** The percentage of T cells responsive to RBD peptide library stimulation in mdLN, including $CD4^+$ and $CD8^+$ T cells. Data are presented as mean ± s.d. Symbols indicate data collected from individual mice. Statistical significance was calculated by one-way ANOVA with Dunnett correction.

168 hours post-administration, weak but detectable 4RBD-Fc signals were also observed in other secondary lymphoid organs, suggesting limited dissemination beyond the respiratory-associated lymphoid tissues at later stages.

We further validated whether 4RBD-Fc draining to respiratory-associated lymphoid tissues could activate local immune responses, including innate and adaptive immunity. We i.n. administered 1 mg of 4RBD-Fc to a group of C57BL/6 mice and collected serum and mdLN at 0, 12, 48, 96, and 168 hours for analysis (Fig. 3D). By 168 hours post-administration, anti-RBD IgG antibodies became detectable in the serum of these mice at a titer of 9.3×10^2 using ELISA (Fig. 3F). Since the activation of B cell responses involves the expansion and differentiation of antigen-specific B cells, we used fluorescence-labeled RBD tetramers and flow cytometry to detect RBD^+ B cells in mdLN (Fig. 3E, G). Robust RBD^+ B cell expansion was detected at 168 hours in mdLN (Fig. 3G), characterized by significant increases in both proportions (1.2% versus 0.05%) and numbers (2×10^4 versus 2×10^2) of RBD^+ B cells (Fig. 3G, H). Through further B cell phenotypic analysis, we observed differentiation in these RBD^+ B cells. The proportion of Naive B cells (Naive, $CD38^+IgD^+$) significantly decreased among RBD^+ B cells at 168 hours (95.2% at 96 hours versus 15.7% at 168 hours). Concurrently, the proportion of Memory B cells (Bmem, $CD38^+IgD^-$) in RBD^+ B cells increased at 96 hours (0% at 48 hours versus 4.1% at 96 hours), and germinal center B cells (GC, $CD38^-IgD^-$) appeared at 168 hours (0% at 96 hours versus 78.9% at 168 hours), suggesting differentiation of RBD^+ Naïve B cells into GC and Bmem (Fig. 3I). These data indicate that i.n. administration of 4RBD-Fc triggered an RBD-specific B cell response in mdLN.

To assess the longevity of the anti-RBD immune response elicited by a single intranasal dose of 4RBD-Fc (1 mg, no adjuvant), we measured serum

IgG endpoint titers at Days 14, 28, 42 and 56 post-administrations (Fig. 3E). Titers at Day 42 showed less than a 20% decline versus Day 14, indicating sustained antibody production. Consistently, serum collected at Day 42 exhibited pseudovirus IC_{50} values statistically indistinguishable from those at Day 14 (Supplementary Fig. 7F), demonstrating persistent functional neutralization capacity. These findings suggest that, although additional long-term follow-up is needed to fully confirm durability, the neutralizing antibody activity remains effective at least up to Day 42 post-immunization, providing evidence for lasting antiviral protection.

To better understand 4RBD-Fc elicited immunity, we investigated the dynamic changes of immune cell subsets within these draining lymph nodes using flow cytometry, including dendritic cells (DCs), and antigen-specific T and B cells. Migratory DCs (tDCs) have been demonstrated to actively collect respiratory antigens and initiate adaptive immunity in mdLN[33,34]. In mdLN, a cohort of tDCs was the first to respond to i.n. 4RBD-Fc, showing a significant increase at 48 hours post-administration (2.3×10^2 at 0 hour versus 1.3×10^3 at 48 hours) (Fig. 3J). By 96 hours, lymph node cells stimulated with an RBD peptide library exhibited a marked increase in IFN-γ^+CD4^+ (0.06% at 0 hour versus 0.32% at 96 hours) and IFN-γ^+CD8^+ T cells (0.06% at 0 hour versus 1.25% at 96 hours), indicating the initiation of a Th1-biased RBD-specific cellular immunity (Fig. 3K). Similar RBD-specific B cell responses were observed in NALT and maLN, but not in the lungs (Supplementary Fig. 6A–F). Together, these findings provide cellular-level evidence that i.n. administration of 4RBD-Fc activates RBD-specific immunity in respiratory-associated lymphoid tissues.

Requirement of both Fc-fusion and antigen dosage for adjuvant-free mucosal immunogenicity of 4RBD-Fc

Typically, protein antigens require adjuvants to activate mucosal immunity[23,35,36]. However, the antiviral formulation of 4RBD-Fc demonstrates the ability to achieve mucosal immune activation without adjuvants, which may attribute to its unique structure or dosage. To investigate the mechanism of this adjuvant-free immune activation, we administered 4RBD-Fc or 3RBD—which is also multimeric but lacks Fc-fusion—at low (lo, 20 μg) or high doses (hi, 1 mg) via i.n. administration in C57BL/6 mice, all without adjuvants. While the mock group received an equal volume of PBS (Fig. 4A). ELISA analysis of mice serum at day 7 revealed that anti-RBD IgG antibodies in the 4RBD-Fc (hi) group has an average titer of 2.5×10^3. Conversely, only 25% (1/4) of mice in 3RBD (lo) and 3RBD (hi) groups showed detectable anti-RBD antibodies at a much lower titer of 1×10^2 (Fig. 4B). These results demonstrated effective anti-RBD antibody response could only be achieved in the 4RBD-Fc (hi) group. Flow cytometry analysis of RBD-specific B cells in 4RBD-Fc (hi) group revealed an RBD-specific GC response and B cell differentiation, marked by an increase in percentages and numbers of RBD^+ B cell (Fig. 4C, D), a decrease in naive B cells (98.1% versus 28.1%), and an increase in GC B cells (0% versus 60%) and Bmem (0.6% versus 5.9%) (Fig. 4E) in mdLN. Meanwhile, only a notably higher frequencies of RBD peptide reactive IFN-γ^+CD4^+ and IFN-γ^+CD8^+ T cells were observed in the 4RBD-Fc (hi) group, compared to all other groups (Fig. 4F, G). Consistently, DC subsets in mdLN were also significantly elevated in the 4RBD-Fc (hi) group (Fig. 4H). This indicating that RBD-specific T cell response are exclusively generated in the 4RBD-Fc hi group. Together, these results suggest that both Fc-fusion and high antigen dosage contribute to the adjuvant-free mucosal immunogenicity of 4RBD-Fc in mice.

Enhanced systemic and mucosal immunity induced by the antiviral formulation of 4RBD-Fc compared to the vaccine formulation

To assess whether the immune response elicited by the antiviral drug formulation of 4RBD-Fc is sufficient to provide viral protection, we first compared it to the immune response induced by a validated mucosal vaccine formulation[23,37–39]. By Fc-fused protein antigens to target the FcRn receptors expressed on respiratory epithelial cells, mucosal vaccines facilitate the crossing of antigens through the mucosal barrier and activate mucosal immunity in the presence of adjuvants[23,24,39]. Since human IgG1-Fc can bind to murine FcRn with similar affinity[24], the 4RBD-Fc construct meets this criterion. Therefore, we developed a mucosal vaccine formulation of 4RBD-Fc (20 μg with CpG adjuvant) and compared the systemic and mucosal immune responses it induced to those triggered by the antiviral drug formulation (1 mg 4RBD-Fc without adjuvant), while the mock group received 20 μg CpG i.n. only (Fig. 5A). Following twice i.n. administration in C57BL/6 mice, both formulations induced respiratory mucosal immunity (Fig. 5B–J), including lung-resident memory B cells (BRMs) (Fig. 5B, H), mucosal antibodies in bronchoalveolar lavage (BAL) (Fig. 5D), GC responses in mdLN (Fig. 5G) and T cells in the lungs (Fig. 5I, J). Notably, the antiviral formulation demonstrated a rapid antibody production, with anti-RBD IgG antibodies detectable in serum by day 7 (6.3×10^3), and consistently surpassed the vaccine formulation at subsequent time points (1.6×10^4 versus 1.3×10^3 at day 14, 6.3×10^5 versus 3.2×10^4 at day 28) (Fig. 5C). Of note, the antiviral formulation induced 10-fold higher mucosal IgG antibodies titer in BAL (9.2×10^3) compared to the vaccine formulation (9.3×10^2) (Fig. 5D, E). At day 28, serum from mice treated with antiviral formulation showed neutralizing activity against WT SARS-CoV-2 pseudovirus ($IC_{50} = 4716$), while the vaccine formulation did not exhibit detectable neutralizing activity (IC_{50} not determined) (Fig. 5F). Flow cytometry analysis revealed that antiviral formulation induced significant more RBD^+ GC B cells in mdLN (2.1×10^3 versus 3.6×10^2) (Fig. 5G). To distinguish lung-resident B cells from circulating B cells, anti-CD45-APC antibody was administered intravenously (i.v.) to label circulating immune cells[40]. Cells that were $CD19^+CD45i.v.^-CD38^+IgD^-$ were considered to be lung-resident memory B cells[41]. The antiviral formulation (1.3×10^3) elicited 8.9-fold more RBD^+ BRMs than the vaccine formulation (1.5×10^2) in the lungs (Fig. 5H). Both formulations induced more RBD-specific T cells in the lungs comparing to the mock group, including IL-2^+ and TNF-α^+CD4^+ (Fig. 5I) and TNF-α^+CD8^+ T cells (Fig. 5J), detected via RBD peptide library stimulation and intracellular cytokine staining. Together, these data demonstrated that when administered intranasally, the antiviral 4RBD-Fc formulation elicits a stronger mucosal and systemic immune response than the vaccine formulation, while the vaccine formulation remains effective via intramuscular administration.

4RBD-Fc antiviral formulation outperforms vaccine formulation in providing immediate and sustained protection against SARS-CoV-2 variant

We postulated that the antiviral formulation of 4RBD-Fc would not only protect mice from imminent infection, as demonstrated in Fig. 2, but also offer sustained protection through its rapid and strong vaccine-like immune activation effect. As such, we compared the protectivity of 4RBD-Fc in antiviral formulation with vaccine formulation against SARS-COV-2 challenge (Fig. 6A). The vaccine group of K18-hACE2 mice was primed with 20 μg 4RBD-Fc adjuvanted with CpG i.n. at day 0, followed by two subsequent boosters at day 14 and day 42, then exposed to a lethal dose of SARS-CoV-2 Delta strain (4×10^3 PFU) at day 63. Equal volume of PBS containing CpG i.n. was used as mock treatments. The antiviral group of K18-hACE2 mice received a single dose of 1 mg 4RBD-Fc i.n. at day 0 and were exposed to one lethal dose of SARS-CoV-2 Delta strain (4×10^3 PFU) either at day 7 (D7) or day 14 (D14), or twice at both day 0 and day 14 (D7 + D14) (Fig. 6A). Both formulations effectively shielded K18-hACE2 mice from lethal Delta strain exposures, contrasting with the CpG i.n. group: 16.9% body weight loss and succumbed by 5 dpi (Fig. 6B). Remarkably, the antiviral formulation group, challenged with the Delta strain on either day 7 or day 14 post-administration, maintained stable body weights (100.4-100.7% of starting weight) (Fig. 6B) and exhibited significantly reduced respiratory viral loads (79-fold reduction in throat swaps and 398-fold in lungs) compared to the CpG i.n. group (Fig. 6C, D). Of note, even after two lethal challenges with the Delta strain on Day 0 and Day 14, mice receiving a single dose of the antiviral formulation survived and maintained stable body weights (105% of starting weight) (Fig. 6B). Compared to the CpG i.n. group, these mice exhibited a significant reduction in viral loads in both the upper (1.5×10^5 versus 1.2×10^3 copies/ml) and lower (2.7×10^6 versus $9 \times$

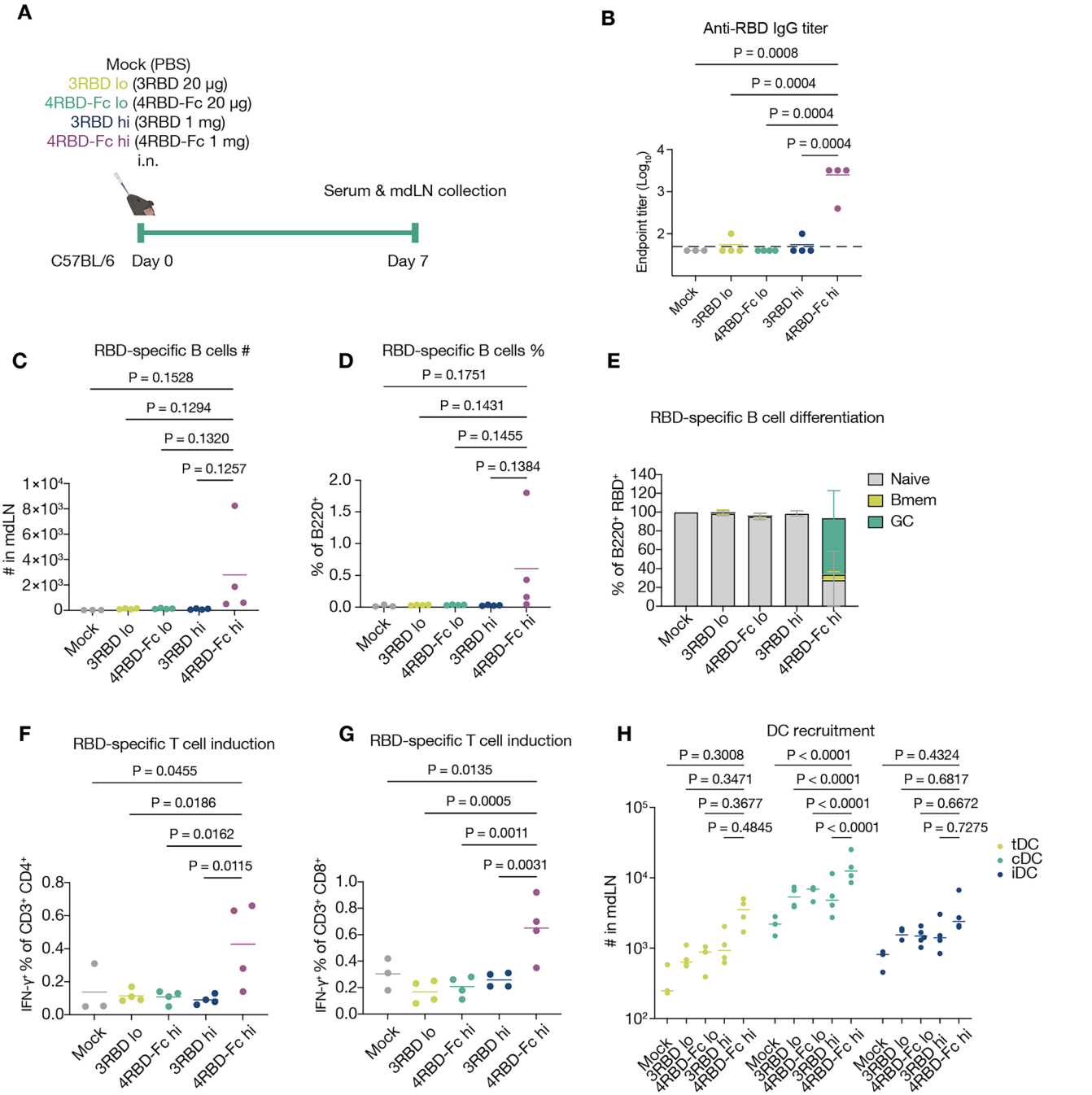

Fig. 4 | Fc-fusion and antigen dosage contribute to the unadjuvanted mucosal immunogenicity of 4RBD-Fc. A Experimental design evaluating whether dosage or structure affects the mucosal immunogenicity of unadjuvanted 4RBD-Fc ($n = 4$). **B** Serum anti-RBD IgG antibodies titers among different antigen and dosage treatment, measured by ELISA. The dashed line indicates the limit of detection (LOD). Undetectable values were set to LOD − 0.2 log units to distinguish them. Quantitative analyses of RBD-specific B cell responses in mdLN, including numbers (**C**) and percentages (**D**) of RBD$^+$ B cells, as well as their differentiation status (**E**). The percentage of pulmonary T cells responsive to RBD peptide library stimulation, including CD4$^+$ (**F**) and CD8$^+$ T cells (**G**). **H** DC subsets in mdLN following i.n. administration of indicated antigen: cDC (MHC-II$^+$CD11c^{hi}), iDC (MHC-II$^+$CD11c^{lo}), tDC (MHC-II^{hi}CD11c$^+$). Data are presented as mean ± s.d. Symbols indicate data collected from individual mice. Statistical significance was calculated by one-way ANOVA with Dunnett correction.

10^3 copies/ml) respiratory tracts (Fig. 6C, D). Given the amount of 4RBD-Fc in the lung was decreased by 50.4-fold at 168 hours post-administration (Fig. 2B), these results suggested that the protective effect of antiviral formulation, initially derived from hACE2 blockade, and followed by the activation and presence of anti-RBD immunity.

Both formulations of 4RBD-Fc markedly curtailed viral replication in throat swabs and lungs (Fig. 6C, D). The pulmonary virus titer assay showed a significant reduction in mice administered with i.n. vaccine formulations (21-fold), compared to the mock groups. However, a greater reduction was observed in those given the antiviral formulation: 735-fold in the D7 group, 191-fold in the D14 group, and 274-fold in the D0 + D14 group, compared to the CpG i.n. group. These data demonstrated that a single dose of antiviral formulation outperformed three rounds of vaccine formulations in reducing viral load in the lower respiratory tract for a sustained period of at least two weeks.

In conclusion, these results demonstrate that the immune responses activated by 4RBD-Fc are sufficient to protect mice from lethal doses of SARS-CoV-2 infection. Moreover, the antiviral formulations of 4RBD-Fc

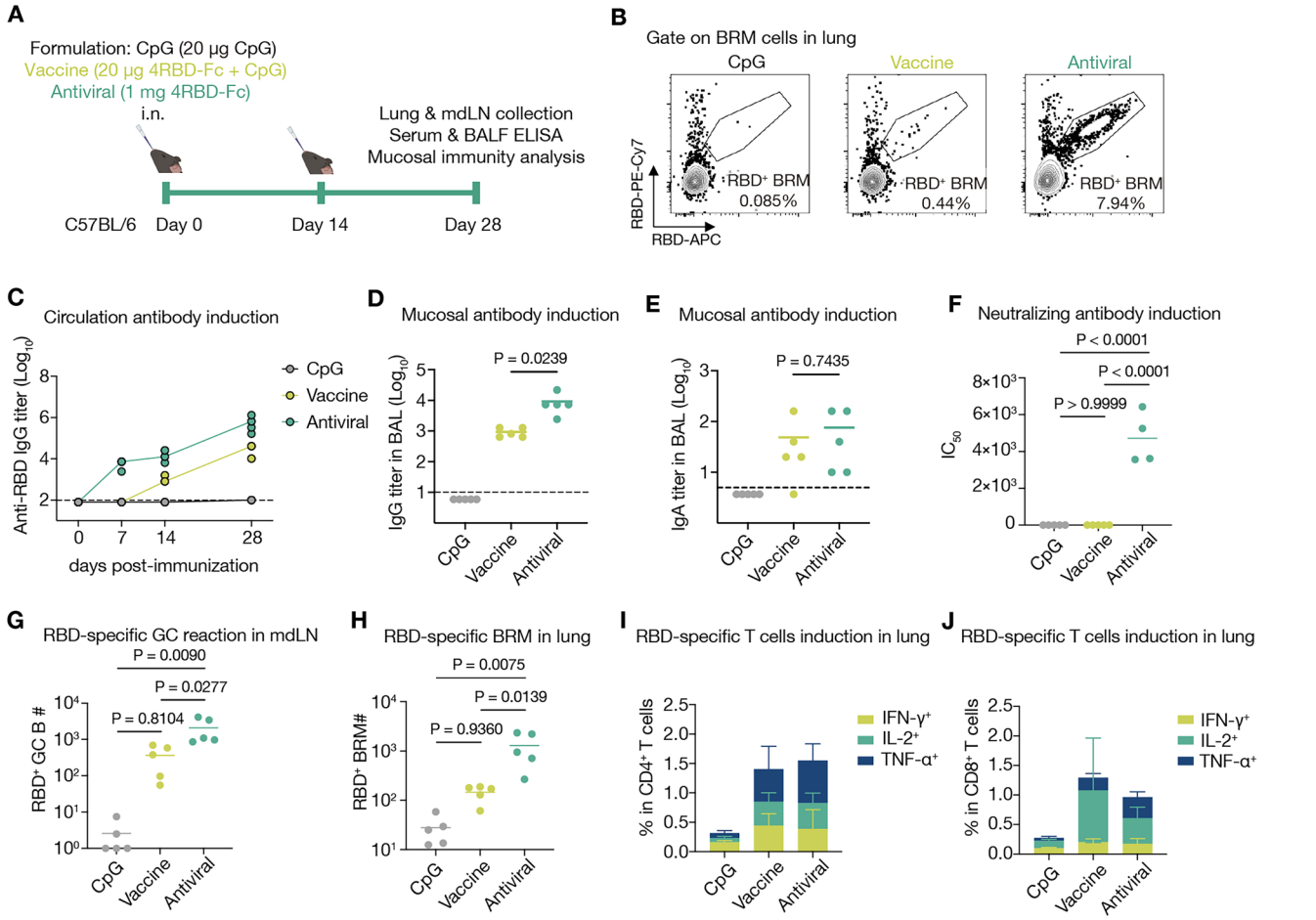

Fig. 5 | The 4RBD-Fc antiviral formulation induced more robust systemic and mucosal immunity than the vaccine formulation. A Illustration of the administration protocol in C57BL/6 mice: Mice were given i.n. 4RBD-Fc vaccine or antiviral formulations, with a booster on day 14. The mock group received 20 μg CpG in PBS ($n = 5$). **B** Representative flow cytometry plots of RBD$^+$ BRMs (CD45i.v.$^-$CD19$^+$CD38$^+$IgD$^-$RBD-FITC$^+$RBD-PE-Cy7$^+$). Cells that were CD45i.v.$^-$CD19$^+$ were defined as lung-resident B cells. ELISA detection of anti-RBD IgG titer in serum (**C**) and BAL (**D**) and anti-RBD IgA in BAL (**E**). **F** Neutralization assay of serum at day 28 using SARS-CoV-2 WT pseudovirus, IC_{50} values are indicated. RBD$^+$ GC B cell counts (**G**) in mdLN and counts of RBD$^+$ BRMs (**H**) in lungs at day 28. The percentage of pulmonary T cells responsive to RBD peptide library stimulation, including CD4$^+$ (**I**) and CD8$^+$ T cells (**J**). Data are presented as mean ± s.d., symbols denote individual data points collected from mice. The dashed line indicates the limit of detection (LOD). Undetectable values were set to LOD −0.2 log units to distinguish them. Statistical significance was calculated by one-way ANOVA with Dunnett correction.

offer superior protection to the lungs compared to vaccine formulations. Particularly, the dual benefits of immediate hACE2 blocking effects and the subsequent development of anti-RBD immunity can be attained with just a single dose of the antiviral formulation of 4RBD-Fc.

Lower dose 4RBD-Fc maintains respiratory tract retention and induces anti-RBD immune responses

To further assess the optimal therapeutic dose of i.n. 4RBD-Fc, we conducted biodistribution and immunogenicity studies using lower doses (50 μg and 200 μg). In vivo imaging and ex vivo organ analysis on day 7 post-administration showed that mice receiving 200 μg of 4RBD-Fc-AF750 retained a greater fluorescent signal in the respiratory tract (nasal cavity and lungs) compared to the 50 μg group (Supplementary Fig. 7A–C). Moreover, lower background signal was observed in peripheral organs in the 200 μg group relative to the original 1 mg dose used in earlier experiments, indicating improved respiratory specificity at the reduced dose.

To determine whether these lower doses could still elicit an immune response, we measured serum anti-RBD IgG titers at day 7 following intranasal administration of unadjuvanted 4RBD-Fc. We found that 200 μg, but not 50 μg, was sufficient to induce a robust antibody response (Supplementary Fig. 7D, F). These results support the use of 200 μg as an effective and respiratory-specific intranasal dose that maintains both local retention and immunogenic potential.

Discussion

Our study presents proof-of-concept and preclinical data demonstrating the feasibility of using viral RBDs as antiviral drugs. By multimerizing and Fc-fused the RBD of SARS-CoV-2, we enhanced its binding affinity to the viral receptor and enabled it to activate the mucosal immune system. This design allows the immune system to take over the short-term protection provided by receptor blocking, resulting in long-term protection from a single-dose administration. We therefore define "durable protection" not merely as the pharmacologic persistence of 4RBD-Fc, but as the extended interval of vaccine-like immunity that persists long after the protein has been cleared from the respiratory tract. Such an approach maximizes the cost-effectiveness of single-dose antiviral interventions, potentially improving medication adherence and overall antiviral outcome.

We postulate two criteria for viral RBD to be developed into antiviral drugs similar to 4RBD-Fc. First, the recombinantly expressed viral RBD should possess enhanced receptor-binding capabilities. Second, it can serve as a potent immunogen to elicit neutralizing antibodies. Viruses such as influenza, rabies, hepatitis C, respiratory syncytial virus, and herpes simplex virus could potentially be adapted to this 4RBD-Fc design to create antiviral

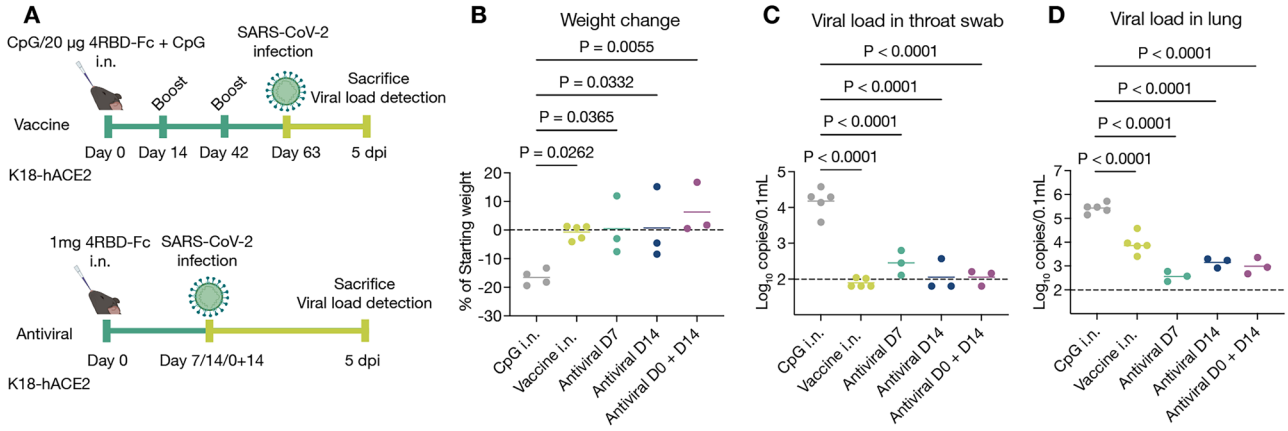

Fig. 6 | Antiviral formulation of 4RBD-Fc provides superior and sustained protection against SARS-CoV-2 compared to vaccine formulation. A Vaccine immunization protocol for K18-hACE2 mice challenged with SARS-CoV-2 Delta strain. Mice were primed i.n. or i.m. with 4RBD-Fc and adjuvant, boosted at days 14 and 42, and challenged with 4×10^3 PFU at day 63. Mock groups received only adjuvant ($n = 5$). For antiviral formulations, mice were i.n. administered 1 mg 4RBD-Fc, then challenged with SARS-CoV-2 Delta strain (4×10^3 PFU) on days 7 and 14 (single challenge) or on days 0 and 14 (twice challenges) ($n = 3$). **B** Relative weight was measured as a percent of the starting weight on day 5 after infection with SARS-CoV-2 Delta strain. The dashed line indicates the starting weight. **C, D** Viral loads in throat swabs (**C**) and lungs (**D**), assessed by qRT-PCR. The dashed line indicates the limit of detection (LOD). Undetectable values were set to LOD −0.2 log units to distinguish them. Data are presented as mean ± s.d., symbols denote individual data points collected from mice. Statistical significance was calculated by one-way ANOVA with Dunnett correction.

agents. Meanwhile, as primary sites of infection for these viruses are not restricted to the respiratory tract but rather blood, nerves, genital mucosa, and other tissues, alternative delivery methods, such as injection at the site of an animal bite, intravenous administration, or mucosal gels need to be evaluated for viral infection blocking and immune activation.

In the first week post administration, 4RBD-Fc targets the ACE2 receptor, endowing it with broad-spectrum activity against SARS-CoV-2 and reducing susceptibility to viral mutations[42]. Moreover, the rapid onset of mucosal immunity by 4RBD-Fc antiviral formulation results in a minimum two-week enduring antiviral effect immediately after the administration. These advantages implies that a single inhalation of 4RBD-Fc may provide sustained prophylactic benefits against the threat of emerging virus. Compared to repetitive vaccine boosters or daily antiviral drug administration, 4RBD-Fc can reduce medical resource utilization and improve adherence, thereby enhancing antiviral effectiveness and transmission control[43,44]. Although ACE2-blocking antibodies can achieve similar effects in blocking ACE2[45,46], repeated use of such antibodies may lead to anti-drug antibody responses, diminishing their effectiveness. This type of resistance does not occur with 4RBD-Fc, as antibodies generated against 4RBD-Fc could instead offer antiviral protection. These characteristics underscore the advantages of 4RBD-Fc as an antiviral agent in terms of breadth of action, duration of effect, and resistance profile.

In the context of immune activation by 4RBD-Fc, it functions as a mucosal vaccine, addressing a crucial gap in current vaccine development strategies. While most existing vaccines focus on reducing mortality and disease severity by inducing systemic immunity, they often fail to elicit adequate mucosal immunity[47,48], a critical shortfall considering the majority of viruses infecting humans invade through mucosal surfaces[19]. Traditional i.m. vaccines do not effectively generate mucosal antibodies, BRMs[41,49], and trained macrophages[50], which are essential for preemptive defense against these pathogens and could break the chain of transmission. A single i.n. administration of 4RBD-Fc provided enhanced protection compared to multiple vaccinations, likely due to the generation of anti-RBD mucosal antibodies, BRMs, and pulmonary T cells.

We have noted recent reports suggesting that mucosal immunity can be induced via intranasal administration of adjuvant-free spike or RBD-hemagglutinin (RBD-HA) proteins following a priming immunization with an adjuvanted intramuscular vaccine. This approach serves as a mucosal booster to complement the lack of mucosal protection from intramuscular vaccinations[21,38]. Interestingly, we found that 4RBD-Fc could induce de novo mucosal immune responses without prior immunization. In contrast, RBD-HA proteins rely on pre-existing anti-HA IgG to induce RBD-specific antibodies[38], and the formation of immune complexes between RBD-HA and anti-HA IgG is speculated to facilitate the crossing of the mucosal barrier via the FcRn receptor on respiratory epithelial cells, thereby enhancing dendritic cell activation and antigen uptake. Our 4RBD-Fc construct likely mimics the features of immune complexes, with the Fc-fusion and high antigen valency being crucial for induction of anti-RBD responses. Furthermore, the preferential draining and accumulation of 4RBD-Fc in the mediastinal lymph nodes (mdLN) might also contribute to the initiation and persistence of GC responses, as the amount of antigen dictates the magnitude of GC responses and bronchus-associated memory B cells originate from GCs in mdLN[41,51]. Given these properties, it would be of interest in future studies to evaluate the efficacy of 4RBD-Fc in animals with pre-existing anti-RBD antibodies, as pre-existing immunity could potentially influence antigen handling, mucosal transport, and subsequent immune activation. As such, our design of 4RBD-Fc as an immunogen might advance the development of adjuvant-free mucosal vaccines.

In summary, we demonstrated that rational design of RBD-based antivirals, 4RBD-Fc as an example, could confer long-term protection against viral infection with a single-dose administration through viral entry blockade and anti-viral immune activation. Immune responses elicited by such a design are characterized by high titers of circulating and mucosal antibodies and featured with more BRMs than multiple rounds of adjuvanted immunizations. Extension of this strategy to other viral membrane fusion proteins may accelerate the development of long-acting, single-dose antiviral drugs.

Methods

Study design

We have complied with all relevant ethical regulations for animal use. All experiments involving the immunization and generation and characterization of mice were approved by an Institutional Animal Care and Use Committee (IACUC) of Nanjing University (AP# LY-01). The Ethics Committee of Zhongshan School of Medicine of Sun Yat-sen University on Laboratory Animal Care (SYSU-IACUC-2021-00432) approved all virus infection experiments and was guided by the Laboratory Monitoring Committee of Guangdong Province of China. For anesthesia, mice were administered 1.25% avertin via intraperitoneal (i.p.) injection. Mice were euthanized by CO_2 asphyxiation. C57BL/6, BALB/c, and B6/JGpt-H11em1Cin(K18-hACE2)/Gpt mice (K18-hACE2 mice, Strain No.

T037657) at 8-12 weeks age old were purchased from GemPharmatech. Randomization was performed by assigning mice of the same strain, weight, and age into groups randomly, and administering mice in the same treatment groups randomly with reagents aliquoted from the same stock vial. Both male and female mice were used in experiments.

Statistics and Reproducibility

All statistical analyses were performed using GraphPad Prism 9.0 (GraphPad Software, San Diego, CA, USA). Prior to statistical testing, data were assessed for normality using the Shapiro–Wilk test. For normally distributed data, unpaired t-tests were used for comparisons between two groups, and one-way ANOVA followed by Dunnett's multiple comparisons test was applied for comparisons among more than two groups. For non-normally distributed data, the Mann–Whitney U test was used for two-group comparisons, and the Kruskal–Wallis test followed by Dunn's post-hoc test was applied when comparing more than two groups. All tests were two-tailed, and p values < 0.05 were considered statistically significant. Each experimental group included at least three biological replicates.

For qRT-PCR assays, both positive and negative controls using simulated RNA virus particles were included to monitor the integrity and reliability of the entire experimental process. In competitive cell-surface binding assays, IC_{50} values were determined by fitting a non-linear three-parameter inhibitor-response curve in GraphPad Prism and subsequently converted to the absolute inhibition constant (K_d) using the Cheng–Prusoff equation. IC_{50} values in neutralization assays were similarly calculated using a non-linear regression model.

Gene cloning, protein expression, and purification

RBD (residues 319-591 of the SARS-COV-2 spike protein) containing a C-terminal 8×His tag in pcDNA3.4 modified vector, was synthesized by GenScript. Indicated number of RBD domains were connected in series to form 2RBD and 3RBD. RBD-Fc, 2RBD-Fc, 3RBD-Fc and 4RBD-Fc were composed of the indicated number of RBD connected in series with a Fc domain of human IgG1. Construct sequences were all verified by direct DNA sequencing (General Biol). All RBD proteins were expressed in Expi293 cells (OPM Biosciences) with serum-free medium of OPM-293 CD05 (OPM Biosciences, P688293). For protein purification of RBD proteins with His-tag, culture supernatant was passed through a Ni-NTA affinity column (Sepax-tech, 280660950), and Fc-tag RBD proteins were purified using a protein affinity A column (Sepax-tech, 271120980). Proteins were further purified by gel filtration (SuperdexTM 200 Increase 10/30GL, GE Healthcare), and determined by SDS-PAGE and Coomassie blue staining. 4RBD-Fc was labeled with AlexaFluor 750 using an NHS-ester reaction. The protein was incubated with AlexaFluor 750-NHS (Thermo Fisher, A20111) in a 3:1 molar ratio for 2 hours at room temperature. Unbound dye was removed by ultra-centrifugal filtration using a 30 kDa cut-off filter. The purity and conjugation were confirmed by SDS-PAGE analysis.

Competitive cells-surface binding

Competitive cells-surface binding was performed using RBD protein labeled with AlexaFluor488 NHS Ester (Yeasen, 40779ES03) according to the manufacturer's instructions. 293T-hACE2 cells were resuspended in PBS buffer and incubated with 100 nM AlexaFluor488 labeled-RBD in the presence of competitors (unlabeled-RBD proteins). The decrease of MFI value was directly proportional to the increase in the concentration of competitors. Competition curves were fitted using nonlinear regression with the top and bottom values shared.

Negative staining electron microscopy (EM)

4RBD-Fc protein (100 μg/ml) in 20 mM Tris buffered saline (pH 7.4) was subjected to Superdex 200 gel filtration. Peak fractions were applied to glow-discharged grids, stained with 0.2% (wt/vol) uranyl acetate, and imaged with an Talos L120C G2 microscope and CCD camera at 57,000 × magnification (1.93 Å pixel size) and -2.5 μm defocus.

Molecular dynamics (MD) simulation

The two candidate RBD molecule were submitted to MD to examine the stability using Nanoscale MD (NAMD) and analysis by Visual Molecular Dynamics (VMD). PDB format files were cut off from SARS-CoV-2 spike glycoprotein (PDB ID: 6VXX), NAMD input files were generated through psfgen tool. In order to approach the physiological situation, system was solvated using the TIP3P water model and neutralized with NaCl to an ionic concentration of 0.15 M. We applied the following simulation protocols for two system equally: 35 ps minimization by steepest decent method; 2 ns restrained simulation with gradually decreasing force constant coefficient (0.5, 0.1, 0.025, 0.008, 0.004) to maintain initial structure, then followed by unrestrained 100 ns production MD with time step 2 fs. We used a NPT ensemble with standard NAMD simulation parameters. The cutoff distance was 12.0 Å, the switchdist variable was 10.0 Å, and the pairlistdist variable was 14.0 Å. Particle Mesh Ewald (PME) was used to calculate charge interactions. Langevin dynamics were used to control the temperature and pressure. The stability of two RBD molecule was compared by computing the backbone root-mean-squared deviation (RMSD) of the entire trajectories, carried out by VMD software.

Cells and viruses

Vero E6 cells were obtained from ATCC and maintained in Dulbecco's Modified Essential Medium (DMEM) (Thermo Fisher, 11960044) supplemented with 10% fetal bovine serum (FBS) (Thermo Fisher, 26010074) and 1% penicillin–streptomycin (Thermo Fisher, 15140148) at 37 °C with 5% CO2. The ACE2-expression cell line used in the pseudovirus neutralization assay was constructed by transducing 293 T cells with a lentivirus encoding human ACE2 and transmembrane serine protease 2. The WT SARS-CoV-2 virus (GDPCC-nCOV01, GISAID: EPI_ISL_403934), B.1.617.2 (GDPCC 2.00096), and B.1.1.529.2 (GDPCC 2.00299) were obtained from the Guangdong Center for Human Pathogen Culture Collection (GDPCC) at Guangdong Provincial Center for Disease Control and Prevention.

Pseudovirus neutralization assay

For pseudovirus generation, 293 T cells were transfected with psPAX2, pLKO1-Luciferase-P2A-GFP, and pcDNA3.1-Spike (WT or Delta strain) using PEI (Polysciences, 23966). Pseudovirus were obtained from the supernatant 48 hours after transfection. For neutralization assays, 50 μl of pseudovirus (2×10^5 TFU/ml) was mixed with 50 μl of diluted serum and incubated at 37 °C for 30 minutes before being added to 293T-hACE2 cells (MOI = 1). The luminance values were detected using the Firefly Glo Luciferase Reporter Gene Assay Kit (Yeasen, 11404ES60) according to the manufacturer's instructions.

Authentic virus neutralization assay

Vero E6 cells were seeded at a density of 4×10^4 cells/well in 24-well culture plates. Authentic SARS-CoV-2 was added at a MOI of 0.005. 200 μl of serially diluted 4RBD-Fc and authentic SARS-CoV-2 were mixed in medium containing 2% FBS and added to the Vero E6 cells. The culture supernatants were harvested 48 hours post-infection to assess the viral load via qRT-PCR. Non-linear three-parameters inhibitor-response curve using GraphPad Prism 8.0 (GraphPad) was used to determine the IC_{50} values.

Measurement of viral load

For in vitro assay, RNA of culture supernatant was extracted by using TRIzol reagent (Invitrogen, 15596026). For in vivo assay, lungs of SARS-CoV-2-infected mice were collected and homogenized with gentle MACS M tubes (Miltenyi Biotec, 130-093-236) in a gentle MACS dissociator (Miltenyi Biotec, 130-093-235). Then, the total RNA of homogenized lung tissues was extracted with RNeasy Mini Kit (QIAGEN, 74104) according to the manufacturer's instruction. The extracted RNA was performed with qRT-PCR assay to determine the viral RNA copies by using a one-step SARS-CoV-2 RNA detection kit (PCR-Fluorescence Probing) (Da An Gene, DA0931). To generate a standard curve, the SARS-CoV-2 nucleocapsid gene was in vitro transcribed into RNA for standards. Indicated copies of N standards were

10-fold serially diluted and proceeded to qRT-PCR utilizing the same one-step SARS-CoV-2 RNA detection kit to obtain standard curves. The reactions were carried out on a QuantStudio 7 Flex System (Applied Biosystems) according to the manufacturer's instruction under the following reaction conditions: 50 °C for 15 min, 95 °C for 15 min, and 45 cycles of 94 °C for 15 s and 55 °C for 45 s. The viral RNA copies of each tissue were calculated into copies per ml and presented as log10 scale. The N-specific primers and probes were: N-F (5′-CAGTAGGGGAACTTCTCCTGCT-3′), N-R (5′-CTTTGCTGCTGCTTGACAGA-3′) and N-P (5′-FAM-CTGGCAATGGCGGTGATGCTGC-BHQ1-3′).

Evaluation of potential side effects following intranasal administration of 4RBD-Fc

To assess the safety of intranasal administration of 4RBD-Fc, K18-hACE2 mice were monitored daily for general health parameters, including body weight, activity, grooming behavior, and fur condition, for 7 days post-administration. Mice were intranasally administered with 1 mg of 4RBD-Fc or an equal volume of PBS as a vehicle control. Body weight was measured daily, and behavioral observations were conducted in a blinded manner. At 7 days post-administration, lung, spleen, liver, and kidney tissues were harvested for further analyses. Lung single-cell suspensions were prepared for flow cytometric analysis to assess immune cell infiltration and Th2 cell activation after in vitro stimulation with an RBD peptide library. Mice that lost more than 10% of their initial body weight or exhibited signs of distress (hunched posture, ruffled fur, reduced activity) would be considered to have adverse effects, but no such signs were observed in either group.

Protection against SARS-CoV-2 in K18-hACE2 mice

B6/JGpt-H11$^{em1Cin(K18\text{-}hACE2)}$/Gpt (K18-hACE2 mice, Strain NO. T037657) were bought from GemPharmatech and housed under SPF facility in the Model Animal Research Center in Nanjing University (AP# LY-01). The Ethics Committee of Zhongshan School of Medicine of Sun Yat-sen University on Laboratory Animal Care (SYSU-IACUC-2021-00432) approved all virus infection experiments and was guided by the Laboratory Monitoring Committee of Guangdong Province of China. Viral infections were performed in a BSL3 facility in the Zhongshan School of Medicine of Sun Yat-sen University. K18-hACE2 mice were anesthetized with isoflurane and inoculated i.n. with 4×10^3 PFU Delta strain SARS-CoV-2 virus (GDPCC 2.00096) or 1×10^6 PFU Omicron BA.2 strain (GDPCC 2.00299). The lungs were collected at 5 dpi for further assays.

Histopathology

Mice were euthanized, and lungs were isolated and fixed in 4% paraformaldehyde buffer. Lungs were embedded with paraffin. Sections (3–4 μm) were stained with hematoxylin and eosin (HE).

Immunization

For i.n. administration/immunization, each antigen was prepared in a 50 μl mixture diluted with PBS and, where adjuvant indicated, 20 μg CpG ODN 2395 (InvivoGen, tlrl-2395). Mice were anesthetized via i.p. injection of 1.25% avertin prior to administration. Mice in the mock groups received an equal volume of PBS and, where CpG indicated, 20 μg CpG ODN 2395. Mouse's back was kept straight, then add an equal amount of liquid to each nostril, maintaining this position to allow the fluid to flow through the respiratory tract. Trained operators ensured the majority of the fluid entered the lungs through the respiratory tract, minimizing gastric deposition. For i.m. immunization, antigens were diluted in PBS and combined with 50 μl of Aluminum hydroxide gel (InvivoGen, vac-alu-50) and 10 μg CpG ODN 2395. The vaccine was delivered into the gastrocnemius muscle using a 28 G insulin syringe, with the mock groups receiving an equal volume of PBS/adjuvant mixture without antigen. Booster immunizations were applied at the same site using equivalent vaccine doses. For i.p. immunization, antigens, mixed with PBS, were emulsified with 50 μl CFA (Sigma, F5881) using a 25G syringe. The mock groups received an equal volume of PBS emulsified with CFA.

Tracking 4RBD-Fc bio-distribution in mice

After anesthetizing the mice and i.n. administration of 4RBD-Fc-AF750, imaging was performed using the NEWTON 7.0 (VILBER) system (fluorescence ex = 740 nm, em = 800 nm, with consistent aperture and exposure settings). Images were analyzed using Kuant 2.0 software (VILBER), with background fluorescence removed. The background fluorescence was determined by measuring the radiance of the same organs in untreated mice.

RBD peptide library stimulation to detect RBD-specific T cell responses

To characterize T cell immunity against RBD, cells harvested from LN or lung were stimulated with 1 μg/ml RBD peptide library comprising 15 mer peptides overlapping by 11 aa and spanning the entire open reading frame of RBD (319-591) for 6 hours. The peptide library was synthesized by GenScript with more than 85% purity as confirmed by HPLC. Brefeldin A (eBioscience, 00-4506-51) was used as a cytokine secretion inhibitor. For detecting intracellular cytokines in T cells, cells were treated with Cytofix/Cytoperm solution (BD Biosciences, 554714) following the manufacturer's instructions.

RBD-tetramer for analyzing RBD-specific B cell responses

To characterize B cell immunity against RBD, the RBD (319-591) monomer protein was biotinylated using the EZ-Link Sulfo-NHS-Biotinylation Kit (Thermo Scientific, 21425), following the manufacturer's instructions. RBD-biotin was conjugated with streptavidin-FITC (BioLegend, 405202), streptavidin-APC (BioLegend, 405207), or streptavidin-PE-Cy7 (BioLegend, 405206) at a molar ratio of 4:1 at room temperature for 30 minutes to produce fluorescence-labeled RBD-tetramer. Cells harvested from LN or lung were stained with 1 pM RBD-tetramer in 50 μl FACS buffer (2% fetal bovine serum, 2 mM EDTA, 1% penicillin-streptomycin in PBS).

Tissue preparation and flow cytometry

SP and LN cells were minced and filtered on 45 μm filters. Lungs were cut into small pieces and washed of mucus in wash buffer (2 mM EDTA in RPMI-1640), followed by digestion using collagenase D (Sigma, 11088882001) and DNaseI (Sigma, 11284932001) at 37 °C for 30 minutes. Cells were suspended and stained in FACS buffer. Red blood cells were lysed with Red Blood Cell Lysing Buffer (Sigma, R7757). The flow cytometry samples in this article were acquired by a 5-laser Agilent NovoCyte Penteon Flow Cytometer (405 nm Violet, 488 nm Blue, 561 nm Yellow, 637 nm Red, and 349 nm Ultra violet). To distinguish lung-resident lymphocytes from circulating lymphocytes, 5 μg CD45-APC was injected through the tail vein 5 minutes prior to euthanasia. Cells that were CD45-APC i.v.- were considered to be lung-resident cells. Antibodies catalog numbers and dilutions used for flow cytometry include CD45-APC (BioLegend, 103112, 1/50), CD45-BUV395 (BD Biosciences, 563792, 1/50), CD45-BV711 (BioLegend, 103147, 1/50), CD19-BV650 (BD Biosciences, 563235, 1/50), B220-AF488 (BD Biosciences, 557669, 1/50), CD3-FITC (eBioscience, 11-0037-42, 1/50), 7. CD4-APC-eFluor 780 (eBioscience, 47-0042-82, 1/50), CD8-PerCP-Cy5.5 (eBioscience, 45-0081-82, 1/50), CD38-BV421 (BioLegend, 102732, 1/50), IgD-BV786 (BD Biosciences, 563618, 1/50), CD95-BV605 (BioLegend, 152612, 1/50),CD138-PE (BioLegend, 142504, 1/50), IFN-γ-PE (eBioscience, 12-7311-82, 1/50), IL2-BV421 (eBioscience, 48-7021-82, 1/50), IL4-PE-Cy7 (eBioscience, 25-7041-82, 1/50), TNF-α-eFluor 610 (eBioscience, 61-7321-82, 1/50), Ly6G-PerCP-Cy5.5 (BD Biosciences, 560602, 1/50), FcεRIα-Alexa Fluor 647 (BioLegend, 134310, 1/50), CD11c-AF700 (BD Biosciences, 560583, 1/50), F4/80-APC-Cy7 (BioLegend, 123118, 1/50), I-A/I-E(MHC-II)-BV421 (eBioscience, 62-5321-82, 1/50), CD11b-BV605 (BioLegend, 101257, 1/50), NK1.1-BV711 (Biolegend, 108745, 1/50), Ly6c-BV786 (Biolegend, 128041, 1/50), CD64-PE (BD Biosciences, 558455, 1/50), CD127-PE/Dazzle 594 (Biolegend, 135032, 1/50), CD117-PE-Cy7 (eBioscience, 25-1171-82, 1/50) and Fixable Viability Dye eFluor 506 (eBioscience, 65-0866-14, 1/400).

Enzyme-linked immunosorbent assay

Enzyme-linked immunosorbent assay (ELISA) was performed to quantify antigen-specific IgG levels in mouse serum and BAL. Blood samples were centrifuged at 3000 rpm for 10 minutes at 4 °C after coagulation at room temperature for 2 h. Flat-bottom 96-well ELISA plates (NEST, 514201) were coated with RBD protein (25 ng/100 μl/well) overnight at 4°C, blocked with 2% BSA in PBST, and incubated with serial dilutions of serum samples. After washing, bound antibodies were detected with Peroxidase AffiniPure Goat Anti-Mouse IgG (H + L) (Jackson Immuno Research, 115-035-003, 1/1000), followed by TMB substrate development (Sigma, 860336) solution (50 μl/well) for 10 minutes. The reactions were stopped with 50 μl/well of 1.0 M H_2SO_4 stop solution and absorbance measurement at 490 nm.

For each sample, the endpoint titer was defined as the highest dilution that yielded an optical density (OD_{490}) value exceeding the cut-off. The cut-off value was calculated as the mean OD of negative control serum samples (e.g., pre-immune or mock-immunized mice) plus standard deviations (mean + s.d.). All samples were measured in duplicates. Raw OD values were background-corrected by subtracting the mean OD of blank wells (no serum) and accounting for the background signal from negative control sera.

Reporting Summary

Further information on research design is available in the Nature Research Reporting Summary linked to this article.

Data availability

The main data supporting the results in this study are available within the paper and its Supplementary Information. Unedited gel images were presented in the Supplementary Fig. 10. All data generated in this study is available from figshare (https://figshare.com/s/df1ccb0934a7ede53cdc) with the identifier (https://doi.org/10.6084/m9.figshare.28079381).

Received: 1 December 2024; Accepted: 11 August 2025;
Published online: 25 August 2025

References

1. Irvine, C. et al. Efficacy of HIV Postexposure Prophylaxis: Systematic Review and Meta-analysis of Nonhuman Primate Studies. *Clin. Infect. Dis.* **60**, S165–S169 (2015).
2. Ford, N. et al. Choice of antiretroviral drugs for postexposure prophylaxis for adults and adolescents: a systematic review. *Clin. Infect. Dis.* **60**, S170–S176 (2015).
3. Jenness, S. M. et al. Impact of the Centers for Disease Control's HIV Preexposure Prophylaxis Guidelines for men who have sex with men in the United States. *J. Infect. Dis.* **214**, 1800–1807 (2016).
4. Beymer, M. R. et al. Differentiating nonoccupational postexposure prophylaxis seroconverters and non-seroconverters in a community-based clinic in Los Angeles, California. *Open Forum Infect. Dis.* **4**, ofx061 (2017).
5. Fonner, V. A. et al. Safety and efficacy of long-acting injectable cabotegravir as preexposure prophylaxis to prevent HIV acquisition. *AIDS* **37**, 957–966 (2023).
6. Parkin, J. M. et al. Tolerability and side-effects of post-exposure prophylaxis for HIV infection. *Lancet* **355**, 722–723 (2000).
7. Day, S., Mears, A., Bond, K. & Kulasegaram, R. Post-exposure HIV prophylaxis following sexual exposure: a retrospective audit against recent draft BASHH guidance. *Sex. Transm. Infect.* **82**, 236–237 (2006).
8. Lunding, S. et al. The Danish PEP Registry: Experience With the Use of Postexposure Prophylaxis (PEP) Following Sexual Exposure to HIV From 1998 to 2006. *Sex. Transmit. Dis.* **37**, 49–52 (2010).
9. Foster, R. et al. Single-Tablet Emtricitabine-Rilpivirine-Tenofovir as HIV Postexposure Prophylaxis in men who have sex with men. *Clin. Infect. Dis.* **61**, 1336–1341 (2015).
10. Valin, N. et al. Evaluation of tolerability with the co-formulation elvitegravir, cobicistat, emtricitabine, and tenofovir disoproxil fumarate for post-HIV exposure prophylaxis. *BMC Infect. Dis.* **16**, https://doi.org/10.1186/s12879-016-2056-3 (2016).
11. Casasnovas, J. M. Virus-receptor interactions and receptor-mediated virus entry into host cells. *Subcell. Biochem* **68**, 441–466 (2013).
12. Pert, C. B. et al. Octapeptides deduced from the neuropeptide receptor-like pattern of antigen T4 in brain potently inhibit human immunodeficiency virus receptor binding and T-cell infectivity. *Proc. Natl. Acad. Sci. USA* **83**, 9254–9258 (1986).
13. Polianova, M. T., Ruscetti, F. W., Pert, C. B. & Ruff, M. R. Chemokine receptor-5 (CCR5) is a receptor for the HIV entry inhibitor peptide T (DAPTA). *Antivir. Res.* **67**, 83–92 (2005).
14. Li, W., Joshi, M., Singhania, S., Ramsey, K. & Murthy, A. Peptide vaccine: progress and challenges. *Vaccines* **2**, 515–536 (2014).
15. Shang, J. et al. Structural basis of receptor recognition by SARS-CoV-2. *Nature* **581**, 221–224 (2020).
16. Walls, A. C. et al. Structure, function, and antigenicity of the SARS-CoV-2 Spike Glycoprotein. *Cell* **181**, 281–292 e286 (2020).
17. Tong, P. et al. Memory B cell repertoire for recognition of evolving SARS-CoV-2 spike. *Cell* **184**, 4969–4980 e4915 (2021).
18. Premkumar, L. et al. The receptor binding domain of the viral spike protein is an immunodominant and highly specific target of antibodies in SARS-CoV-2 patients. *Sci. Immunol.* **5**, https://doi.org/10.1126/sciimmunol.abc8413 (2020).
19. Wu, C. T. et al. SARS-CoV-2 replication in airway epithelia requires motile cilia and microvillar reprogramming. *Cell* **186**, 112–130 e120 (2023).
20. Oh, J. E. et al. Intranasal priming induces local lung-resident B cell populations that secrete protective mucosal antiviral IgA. *Sci. Immunol.* **6**, eabj5129 (2021).
21. Mao, T. et al. Unadjuvanted intranasal spike vaccine elicits protective mucosal immunity against sarbecoviruses. *Science* **378**, eabo2523 (2022).
22. Batra, S. K., Jain, M., Wittel, U. A., Chauhan, S. C. & Colcher, D. Pharmacokinetics and biodistribution of genetically engineered antibodies. *Curr. Opin. Biotechnol.* **13**, 603–608 (2002).
23. Ye, L., Zeng, R., Bai, Y., Roopenian, D. C. & Zhu, X. Efficient mucosal vaccination mediated by the neonatal Fc receptor. *Nat. Biotechnol.* **29**, 158–163 (2011).
24. Li, W. et al. An FcRn-targeted mucosal vaccine against SARS-CoV-2 infection and transmission. *Nat. Commun.* **14**, 7114 (2023).
25. Spiekermann, G. M. et al. Receptor-mediated immunoglobulin G transport across mucosal barriers in adult life: functional expression of FcRn in the mammalian lung. *J. Exp. Med.* **196**, 303–310 (2002).
26. Huang, Y., Yang, C., Xu, X. F., Xu, W. & Liu, S. W. Structural and functional properties of SARS-CoV-2 spike protein: potential antivirus drug development for COVID-19. *Acta Pharm. Sin.* **41**, 1141–1149 (2020).
27. Han, P. et al. Molecular insights into receptor binding of recent emerging SARS-CoV-2 variants. *Nat. Commun.* **12**, 6103 (2021).
28. Klausberger, M. et al. Designed SARS-CoV-2 receptor binding domain variants form stable monomers. *Biotechnol. J.* **17**, e2100422 (2022).
29. Crawford, K. H. D. et al. Protocol and Reagents for Pseudotyping Lentiviral Particles with SARS-CoV-2 Spike Protein for Neutralization Assays. *Viruses* **12**, https://doi.org/10.3390/v12050513 (2020).
30. Zhou, P. et al. A pneumonia outbreak associated with a new coronavirus of probable bat origin. *Nature* **579**, 270–273 (2020).
31. Winkler, E. S. et al. SARS-CoV-2 infection of human ACE2-transgenic mice causes severe lung inflammation and impaired function. *Nat. Immunol.* **21**, 1327–1335 (2020).
32. Lee, K. S. et al. SARS-CoV-2 Delta variant induces enhanced pathology and inflammatory responses in K18-hACE2 mice. *PLoS One* **17**, e0273430 (2022).
33. Ballesteros-Tato, A., Leon, B., Lund, F. E. & Randall, T. D. Temporal changes in dendritic cell subsets, cross-priming and costimulation via

CD70 control CD8(+) T cell responses to influenza. *Nat. Immunol.* **11**, 216–224 (2010).
34. Vermaelen, K. Y., Carro-Muino, I., Lambrecht, B. N. & Pauwels, R. A. Specific migratory dendritic cells rapidly transport antigen from the airways to the thoracic lymph nodes. *J. Exp. Med* **193**, 51–60 (2001).
35. Bedford, J. G. et al. Unresponsiveness to inhaled antigen is governed by conventional dendritic cells and overridden during infection by monocytes. *Sci. Immunol.* **5**, https://doi.org/10.1126/sciimmunol.abb5439 (2020).
36. Lavelle, E. C. & Ward, R. W. Mucosal vaccines - fortifying the frontiers. *Nat. Rev. Immunol.* **22**, 236–250 (2022).
37. Lei, H. et al. Intranasal administration of a recombinant RBD vaccine induces long-term immunity against Omicron-included SARS-CoV-2 variants. *Signal Transduct. Target Ther.* **7**, 159 (2022).
38. Kawai, A. et al. Intranasal immunization with an RBD-hemagglutinin fusion protein harnesses preexisting immunity to enhance antigen-specific responses. *J. Clin. Invest.* **133**, https://doi.org/10.1172/JCI166827 (2023).
39. Ochsner, S. P. et al. FcRn-targeted mucosal vaccination against influenza virus infection. *J. Immunol.* **207**, 1310–1321 (2021).
40. Anderson, K. G. et al. Intravascular staining for discrimination of vascular and tissue leukocytes. *Nat. Protoc.* **9**, 209–222 (2014).
41. Allie, S. R. et al. The establishment of resident memory B cells in the lung requires local antigen encounter. *Nat. Immunol.* **20**, 97–108 (2019).
42. Li, G., Hilgenfeld, R., Whitley, R. & De Clercq, E. Therapeutic strategies for COVID-19: progress and lessons learned. *Nat. Rev. Drug Discov.* **22**, 449–475 (2023).
43. Torneri, A. et al. A prospect on the use of antiviral drugs to control local outbreaks of COVID-19. *BMC Med.* **18**, 191 (2020).
44. Chavda, V. P., Baviskar, K. P., Vaghela, D. A., Raut, S. S. & Bedse, A. P. Nasal sprays for treating COVID-19: a scientific note. *Pharm. Rep.* **75**, 249–265 (2023).
45. Chen, Y. et al. ACE2-targeting monoclonal antibody as potent and broad-spectrum coronavirus blocker. *Signal Transduct. Target Ther.* **6**, 315 (2021).
46. Du, Y. et al. A broadly neutralizing humanized ACE2-targeting antibody against SARS-CoV-2 variants. *Nat. Commun.* **12**, 5000 (2021).
47. Tang, J. et al. Respiratory mucosal immunity against SARS-CoV-2 following mRNA vaccination. *Sci Immunol*, eadd4853 (2022).
48. Sheikh-Mohamed, S. et al. Systemic and mucosal IgA responses are variably induced in response to SARS-CoV-2 mRNA vaccination and are associated with protection against subsequent infection. *Mucosal Immunol.* **15**, 799–808 (2022).
49. MacLean, A. J. et al. Secondary influenza challenge triggers resident memory B cell migration and rapid relocation to boost antibody secretion at infected sites. *Immunity* **55**, 718–733. e718 (2022).
50. Yao, Y. et al. Induction of autonomous memory alveolar macrophages requires T cell help and is critical to trained immunity. *Cell* **175**, 1634–1650 e1617 (2018).
51. Baumjohann, D. et al. Persistent antigen and germinal center B cells sustain T follicular helper cell responses and phenotype. *Immunity* **38**, 596–605 (2013).

Acknowledgements

We thank the Center for Disease Control and Prevention of Guangdong Province for providing the Delta and Omicron variant of SARS-CoV-2. The schematic diagram was created using BioRender.com Sun, H. (2025) https://BioRender.com/rs736wf. We thank Dr. Yanlei Zhu's insights regarding the 4RBD-Fc structure. This study was supported by grants from National Science and Technology Major Program NO. 2023ZD0500400 (Y.L.), the Fundamental Research Funds for the Central Universities NO.2024300408 (Y.L.), NO.XJ2024003602(Y.L.), NO.020814380191 (X.D.), National Key Research and Development Program of China NO.2020YFA0509000 (X.D.), NO.2020YFA0710800 (X.D.), National Natural Science Foundation of China NO.32471000 (Y.L.), NO.U24A20378 (Y.L.), NO.32171254 (X.D.), NO.82341070 (K.D.), Jiangsu Key Research and Development Program NO.BG2024026 (X.D.), Jiangsu Provincial Science and Technology Plan Special Fund NO.BK20232018 (Y.L.), China Post-doctoral Science Foundation NO.2020T130053ZX (D.R.), and Guangdong Provincial Natural Science Foundation NO.2023A1515011875 (A.H.).

Author contributions

H.S., B.T., D.R., X.D., and Yan L. conceptualized the study and prepared the manuscript. B.T., H.Y., and X.D. designed and generated recombinant RBD proteins. H.S. and Yan L. conceptualized the use of RBD constructs as both antiviral drugs and mucosal vaccines. A.H. and Y.Z. performed clinical isolated SASR-CoV-2-based experiments. B.T., J.C., and T.J. performed cell-surface binding assay and negative staining electron microscopy. H.S., D.R., H.L., Z.Z., Xiang D., W.L., and S.L. performed i.n. administration and immunization experiments. H.S. and H.L. performed the biodistribution and safety assay. H.S. and H.L. constructed a pseudovirus and performed a neutralization assay. Hanri Z., B.K., and Huanying Z. isolated and prepared the virus stock of SARS-CoV-2 B.1.617.2. C.K. and X.P. isolated and prepared the virus stock of SARS-CoV-2 B.1.1.529.2. H.S., B.T., A.H. and D.R. analyzed and interpreted data. H.S. and B.T. wrote the manuscript, and D.R., A.H., Yongzhen L., K.D., X.D., and Yan L. reviewed and edited the manuscript.

Competing interests

The authors declare no competing interests.

Additional information

Supplementary information The online version contains supplementary material available at https://doi.org/10.1038/s42003-025-08704-6.

Correspondence and requests for materials should be addressed to Kai Deng, Xianchi Dong or Yan Li.

Peer review information *Communications Biology* thanks the anonymous reviewers for their contribution to the peer review of this work. Primary Handling Editor: Dario Ummarino. A peer review file is available.